nature biomedical engineering

SUPPLEMENTARY INFORMATION

VOLUME: 1 | ARTICLE NUMBER: 0054

In the format provided by the authors and unedited.

Ultrasensitive tumour-penetrating nanosensors of protease activity

Ester J. Kwon[1,2,†], Jaideep S. Dudani[1,3,†], and Sangeeta N. Bhatia[1,2,4-7,*]

1. Koch Institute for Integrative Cancer Research, Massachusetts Institute of Technology, Cambridge, MA 02139
2. Harvard–MIT Division of Health Sciences and Technology, Institute for Medical Engineering and Science, Massachusetts Institute of Technology, Cambridge, MA 02139
3. Department of Biological Engineering, Massachusetts Institute of Technology, Cambridge, MA 02139
4. Department of Electrical Engineering and Computer Science, Massachusetts Institute of Technology, Cambridge, MA 02139
5. Department of Medicine, Brigham and Women's Hospital and Harvard Medical School, Boston, MA 02115
6. Broad Institute of Massachusetts Institute of Technology and Harvard, Cambridge, MA 02139
7. Howard Hughes Medical Institute, Cambridge, MA 02139

† These authors contributed equally

*Corresponding Author: Sangeeta N. Bhatia
Address: 500 Main Street, 76-453, Cambridge, MA 02142, USA
Phone: 617-253-0893
Fax: 617-324-0740
Email: sbhatia@mit.edu

Table of Contents

Supplemental Text

Description of pharmacokinetic model equations

For complete derivation and description, refer to Kwong et al., PNAS (2015)[1]. Descriptions, equations, and variables are derived from this reference and are included here with discussion of portions relevant for this work.

The model is comprised of five ODEs tracking the levels of nanosensor (substrate tethered onto nanoparticle) and reporters (fragments used for detection) in three compartments (Blood, Tumor, Bladder). The model is deterministic and has several simplifying assumption, such as a well-mixed assumption[1].

After injection, in blood, nanosensors can be depleted by blood proteases (either off-target or secreted proteases from the tumor), diffuse into the tumor, and taken up by the host phagocytic/clearance system. This is described by the following equation:

$$dC_{NP_{Blood}} = -(k_{clear}^{NP}) * \left(C_{NP_{Blood}}\right) - k_{tumor}^{NP} * \left(C_{NP_{Blood}} - C_{NP_T}\right) - \frac{k_{cat}^{MMP9} * E_{MMP9}^{blood} * C_{NP_{blood}}}{\left(K_M^{MMP9} + C_{NP_{blood}}\right)} - \frac{k_{cat}^{blood} * E_{n.s.}^{blood} * C_{NP_{blood}}}{\left(K_M^{blood} + C_{NP_{blood}}\right)} \quad \textbf{(1)}$$

where the first two terms are derived from nanoparticle scaffold half-life and permeability into the tumor and the last two from Michaelis-Menten analysis. In the original derivation, k_{tumor}^{NP}=1.4e-4 min^{-1}, k_{cat}^{MMP9} = 0.5 min^{-1}, and k_{cat}^{blood}=6.6e-2 min^{-1}. These parameters were multiplied by scalar factors of 1.2, 4.0, and 0.03, respectively, to account for the improvements observed in optimization experiments described in **Fig. 2**. Here, we assume that the change in cleavage rates at the highest substrate concentration tested in vitro (6 μM) apply for simplicity, as well generalize the decrease in thrombin cleavage to background blood cleavage.

In the tumor bed, nanosensor concentration increases as they diffuse into the tumor and get depleted as they are cleaved by proteases.

$$dC_{NP_{Tumor}} = k_{tumor}^{NP} * \left(C_{NP_{Blood}} - C_{NP_T}\right) - \frac{k_{cat}^{MMP9} * E_{MMP9}^{tumor} * C_{NP_{tumor}}}{\left(K_M^{MMP9} + C_{NP_{tumor}}\right)} \quad \textbf{(2)}$$

Proteolytic cleavage of nanosensor releases urinary reporters in the tumor that can diffuse back out of the tumor. The change of reporter concentration in the tumor is given by:

$$dC_{R_{Tumor}} = \frac{k_{cat}^{MMP9} * E_{MMP9}^{tumor} * C_{NP_{tumor}}}{\left(K_M^{MMP9} + C_{NP_{tumor}}\right)} - k_{tumor}^{R} * \left(C_{R_{Tumor}}\right) \quad \textbf{(3)}$$

In the blood, reporters can be generated either by proteolytic cleavage in the tumor or by reporters entering from the tumor bed and depleted by clearance, urinary filtration, or non-specific absorption in the kidney.

$$dC_{R_{blood}} = k_{tumor}^{R} * \left(C_{R_{Tumor}}\right) + \frac{k_{cat}^{MMP9} * E_{MMP9}^{blood} * C_{NP_{blood}}}{\left(K_M^{MMP9} + C_{NP_{blood}}\right)} + \frac{k_{cat}^{blood} * E_{n.s.}^{blood} * C_{NP_{blood}}}{\left(K_M^{blood} + C_{NP_{blood}}\right)} - k_{clear}^{R} * \left(C_{R_{Blood}}\right) - k_{absorb}^{R} * \left(C_{R_{Blood}}\right) \quad \textbf{(4)}$$

Reporters from the blood accumulate in the bladder:

$$dC_{R_{Bladder}} = k_{filter}^{R} * \left(C_{R_{Blood}}\right) \quad \textbf{(5)}$$

All starting variables were either fit to experimental data in a mouse model of colorectal cancer or from biochemical assays of proteolysis of our selected substrate[1]. Tumor enzyme concentration was set 700 nM for a 10-mm tumor and 7 nM for a 5-mm tumor. This estimation was arrived at by measuring MMP9 secretion rates of four human colorectal cancer cell lines[1]. The concentration of MMP9 in blood is modeled as one-tenth of tumor concentration based on previous estimation of protein secretion into blood from tumors[2].

For control urine signal, the tumor compartment and all associated variables are omitted. Detection signal is defined as tumor – control urine signal.

The core skeleton code has been deposited on GitHub (https://github.com/jaidud3/Cancer-activity-based-nanosensor-mathematical-framework). The code was run in MATLAB R2013b.

Supplemental Figures

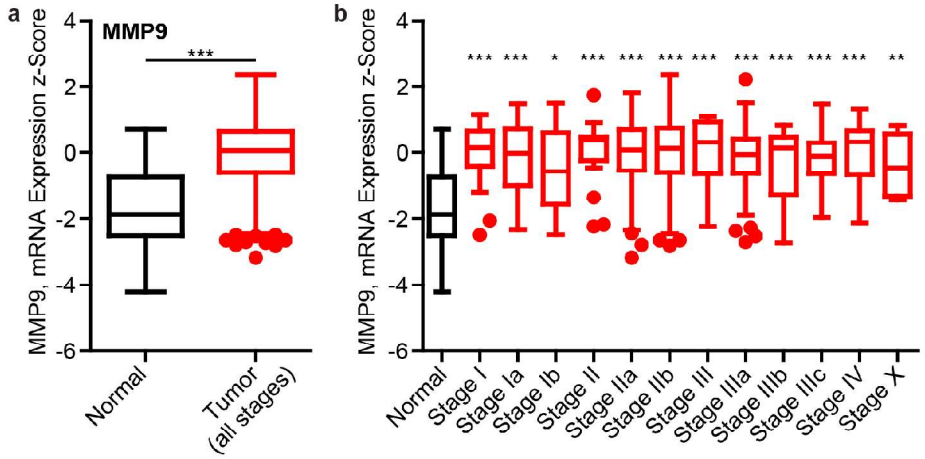

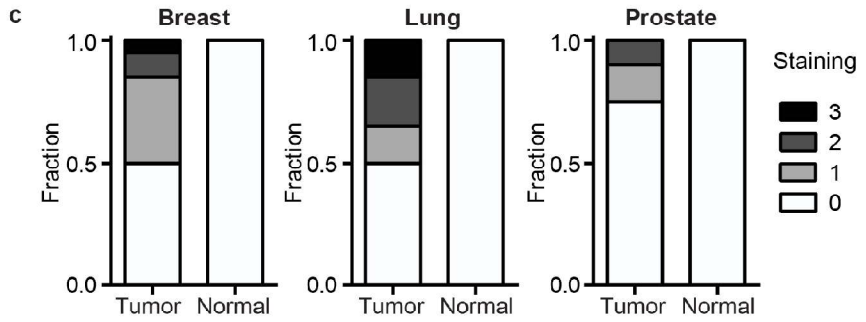

d

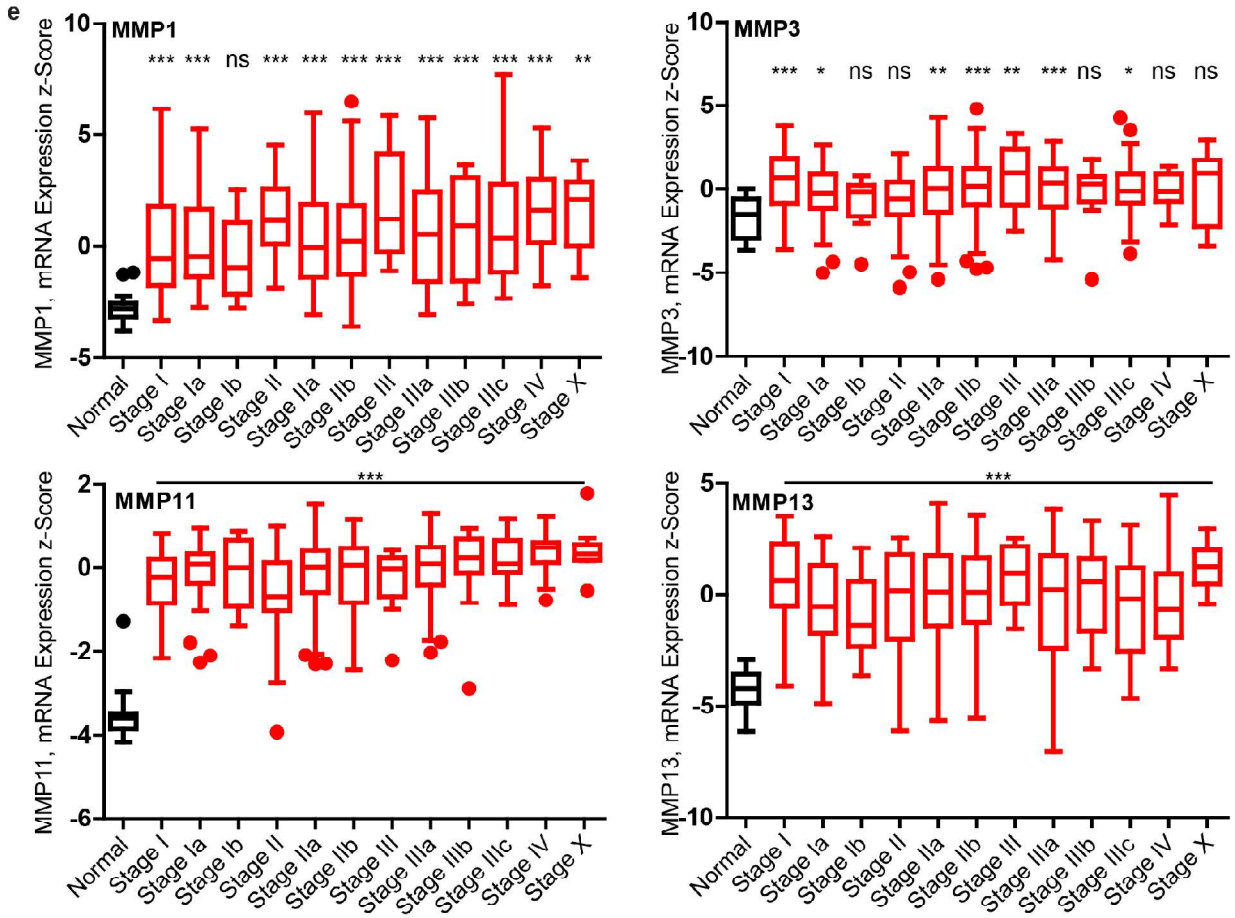

Figure S1. TCGA mRNA and human tissue microarray analysis of MMP9 expression. (**a**) mRNA expression of MMP9 is elevated in breast cancer samples compared to normal adjacent tissue based on analysis from The Cancer Genome Atlas. (**b**) MMP9 mRNA is elevated across all stages of breast cancer compared to normal adjacent tissue based on analysis. (**c**) Scoring of MMP9 staining in tumor and normal tissue from ovarian, breast, lung, and prostate. Cores were scored by a pathologist in a blind manner. (**d**) Scan of tumor microarray stained with MMP9 antibody. Tumor microarray was purchased from US BioMax, Inc. (Catalog No. MC5003b) and full map can be found on their website. (**e**) Several MMPs showed significantly upregulated expression across breast cancer stages compared to normal adjacent tissue (Two-tail Student's t test for **a;** 1way ANOVA with Dunnet's posttest for **b** & **e**; *P<0.05, **P<0.01, ***P<0.001; n = 22 for normal, 39 for Stage I, 42 for Stage Ia, 9 for Stage Ib, 26 for Stage II, 164 for Stage IIa, 103 for Stage IIb, 10 for Stage III, 65 for Stage IIIa, 13 for Stage IIIb, 19 for Stage IIIc, 13 for Stage IV, 9 for Stage X).

For data in **Fig. 1a,** the following cancers were analyzed: Head and Neck (Ginos et al., Cancer Res 2004; 13 normal, 41 tumor), Lung (Bhattacharjee et al., PNAS 2001; 17 normal, 132 tumor), Breast (TCGA; 61 normal, 529 tumor), Glioblastoma (TCGA; 5 normal, 82 tumor), Colon (TCGA; 41 normal, 286 tumor), Ovarian (TCGA; 8 normal, 586 tumor), Prostate (Yu et al., J Clin Oncol 2004; 23 normal, 89 tumor), Liver (Roessler et al., Cancer Res 2010; 220 normal, 225 tumor), Melanoma (Riker et al., BMC Med Genomics; 5 normal, 82 tumor) and Pancreatic (Badea et al., Hepatogastroenterology 2008; 39 normal, 39 tumor).

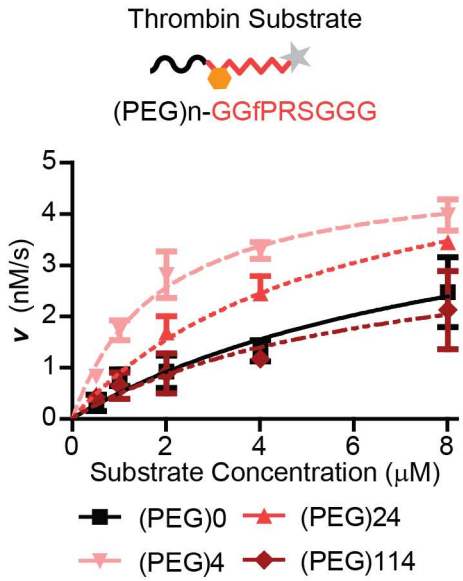

Figure S2. Thrombin cleavage of thrombin substrate varies on surface presentation. A thrombin substrate was presented on the nanoparticle surface with varying linker lengths (n = 2-3, ±SEM). Unlike the MMP substrate, an intermediate length was optimal for thrombin catalysis (see **Fig. 2**). Data was fit to the Michaelis-Menten equation.

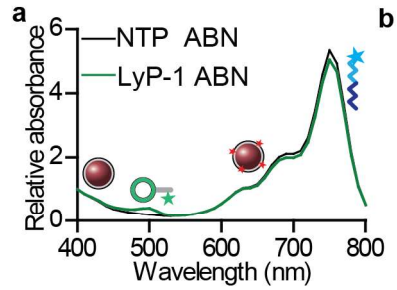

b

Nanoparticle valencies

Name	FAM: NP	VT680: NP	Cy7: NP
NTP	0	12	64.7
LyP-1	4.4	11.6	61.2

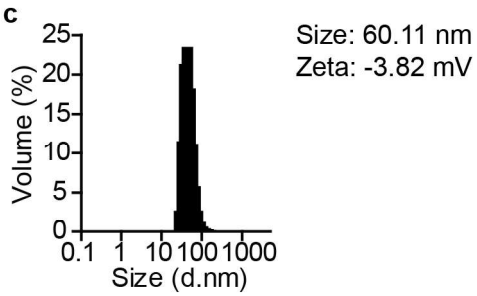

Figure S3. Characterization of targeted vs untargeted nanoparticles. (**a**) Spectra of LyP-1 and non-tumor penetrating (NTP) ABN. Iron oxide absorbs at wavelengths shorter than 400 nm, LyP-1 is tagged with 5FAM dye, the nanoparticle core is labeled with VT-680 and the peptide substrate is labeled with Cy7. (**b**) Peptide substrate valencies were matched between the two nanoparticles. (**c**) Physicochemical characterization of particles by dynamic light scattering shows a hydrodynamic diameter of 60.11 nm and a surface potential of -3.82 mV.

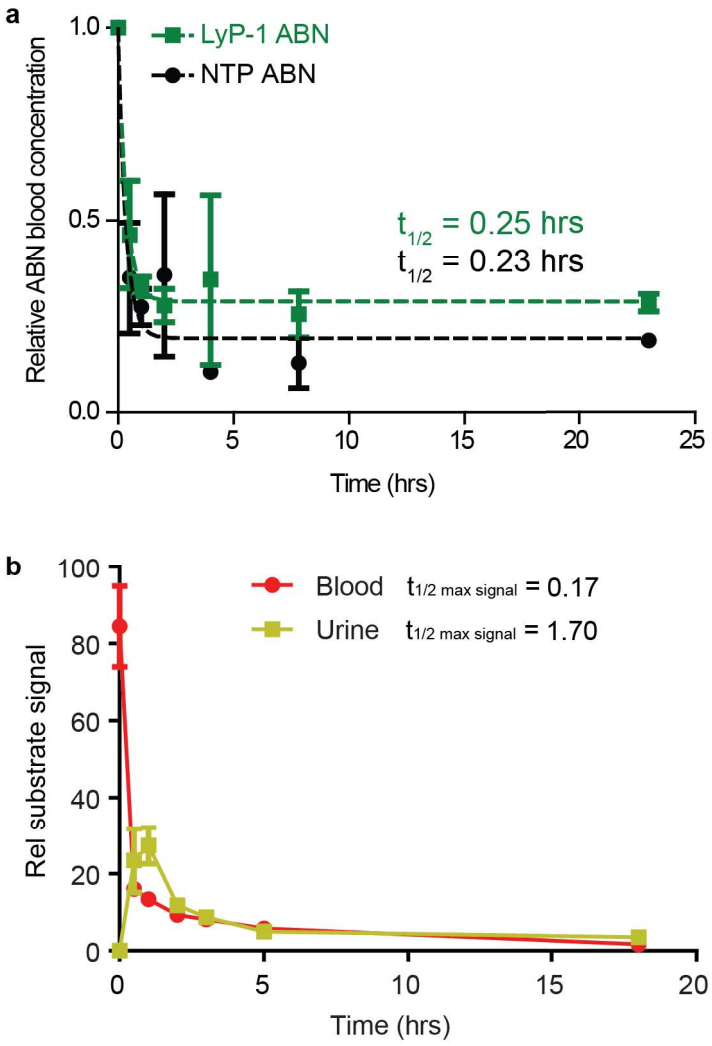

Figure S4. Half-life measurements of ABN and free reporter. (**a**) Blood half-lives of LyP-1 and non-penetrating particles are matched (data fit to one-phase exponential decay). (**b**) Kinetic measurement of the free reporter in the blood and urine after intravenous injection.

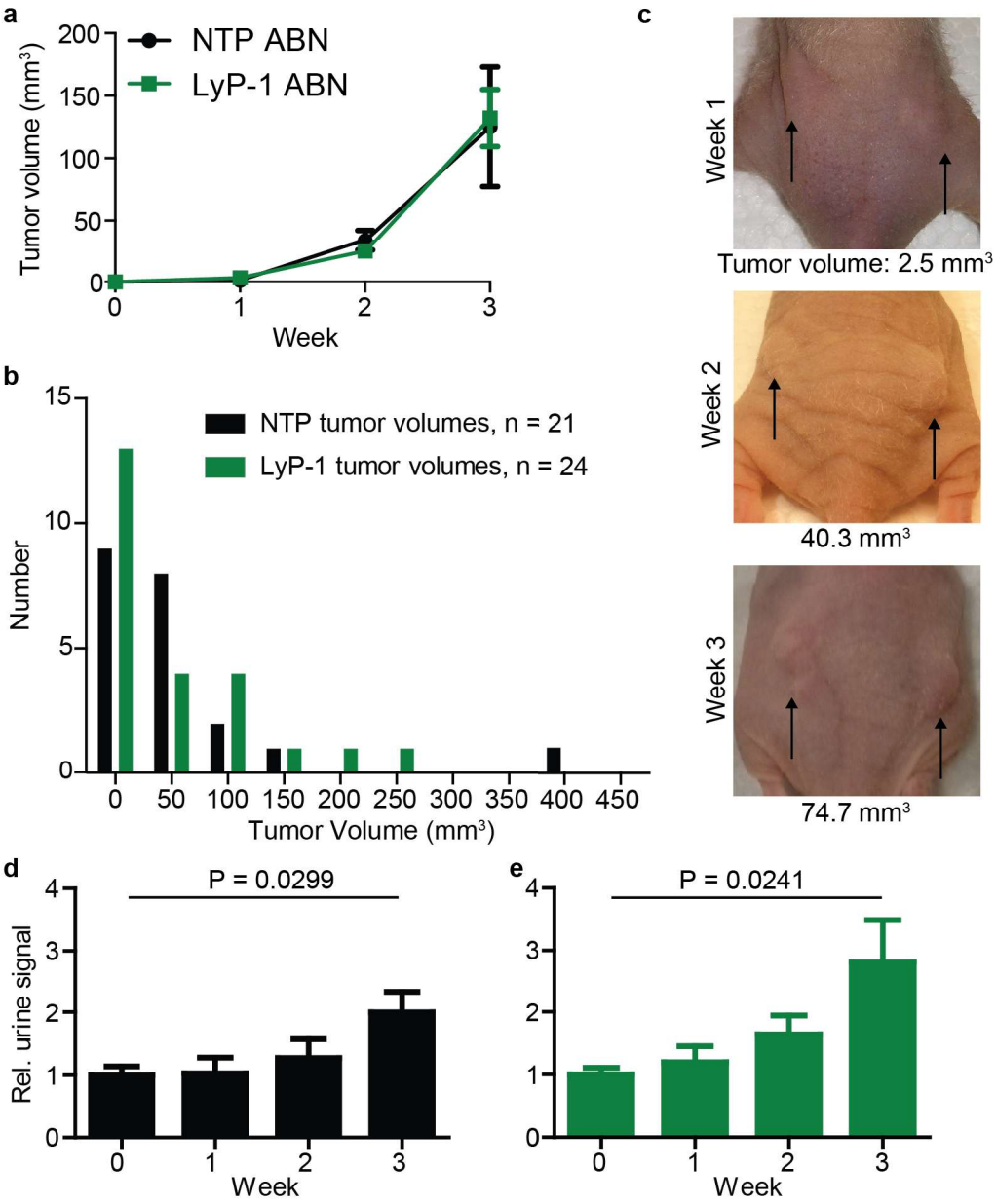

Figure S5. Growth characteristics of MDA-MB-435 flank xenograft. (**a**) Caliper measurements of tumor sizes across both groups were consistent, reaching 100 mm^3 total burden by week 3. (**b**) Histogram of tumor sizes for urine data binning. (**c**) Photographs of flank tumors in nude mice. Targeted synthetic biomarkers were able to classify tumors at week 2. Volumes reported are calculated after measurements performed using a digital caliper. Urine signal for mice administered (**d**) non-penetrating ABNs and (**e**) LyP-1 ABNs over time course of the study (P-value represented on each graph as calculated by repeated measures ANOVA).

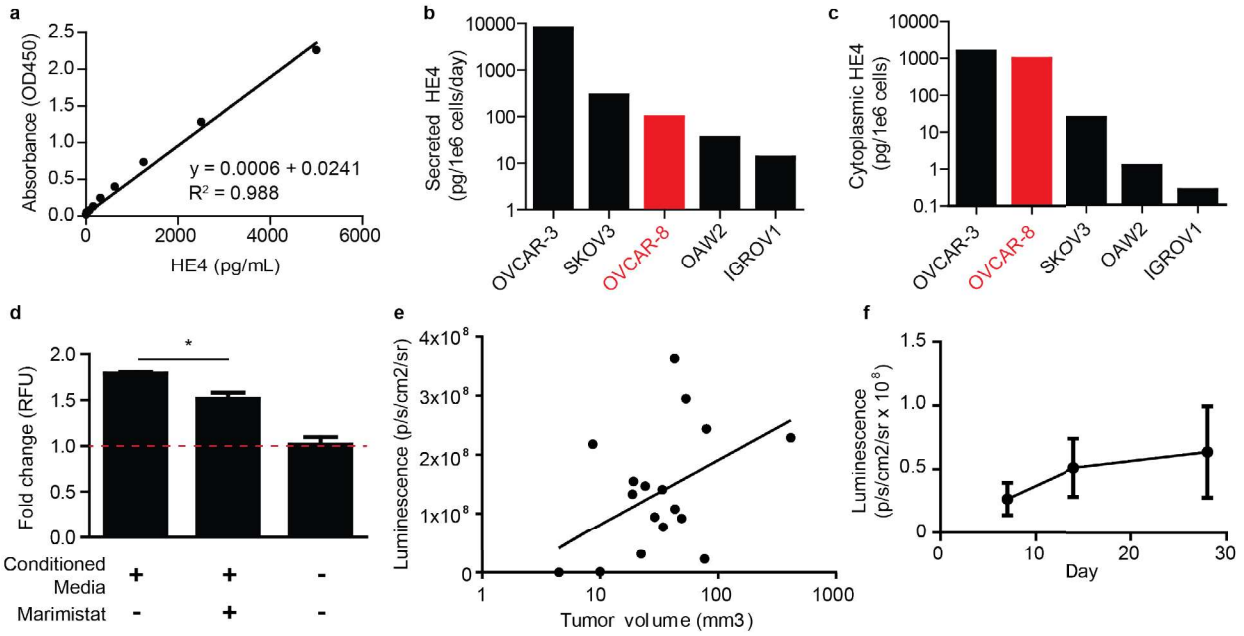

Figure S6. HE4 secretion rates across several ovarian cancer lines. (**a**) Standard curve for the HE4 ELISA. (**b**) Secreted HE4 across several lines was measured by collecting supernatants. Data is normalized to get secretion rate per million cells per day. (**c**) Cytoplasmic HE4 was measured by collecting and lysing cells. OVCAR-8 cells have relatively high secretion and cytoplasmic HE4 compared to cells profiled. (**d**) Cleavage of MMP9 substrate by conditioned media collected from OVCAR-8 cells with and without the MMP inhibitor, Marimistat. Marimistat can inhibit a significant portion of the cleavage. (**e**) Correlation of tumor volumes as measured by imaging of retrieved nodules after necropsy versus bioluminescence imaging. Although there is positive correlation (Spearman r = 0.48, P = 0.04), luminescence can be inaccurate for individual mice due to depth of tumors in the abdomen. (**f**) Bioluminescence imaging shows that on average, tumor burden increases over time.

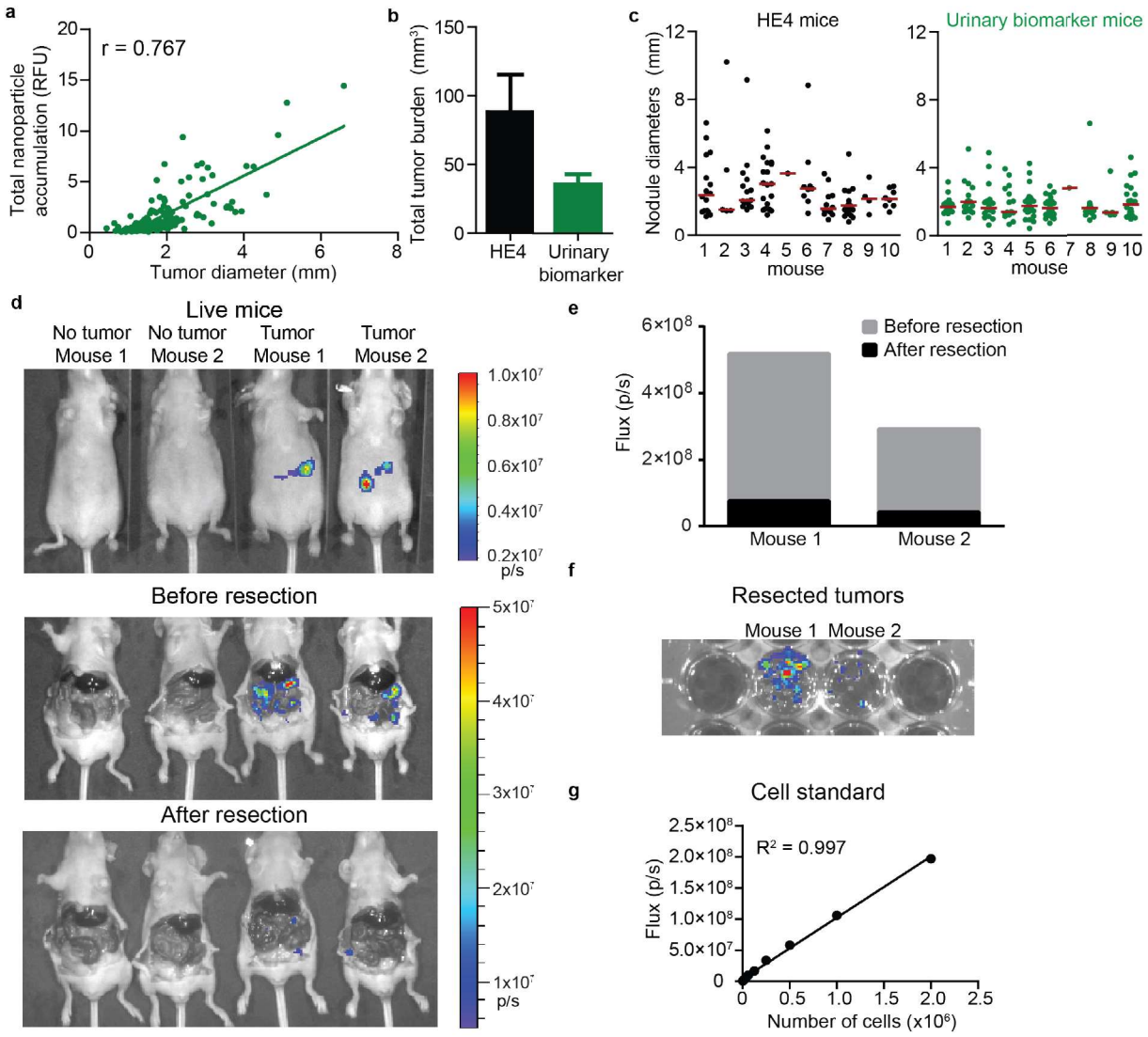

Figure S7. Urinary biomarker performance in the ovarian cancer model. (**a**) Plot of LyP-1 ABN accumulation, as measured by fluorescence intensity, and tumor diameter from the 10 mice shown in **Fig. 4f.** Linear regression shows that total nanoparticle accumulation was correlated with size of individual tumor nodules (Pearson's r = 0.767). (**b**) Total tumor burden was measured at the time when detection became statistically significant for blood biomarker (n = 10, 3 weeks; HE4) or for the urinary biomarker (n=10, 2 weeks). The limit of detection for LyP-1 ABN was at a tumor volume of 36 mm^3 while the limit of detection for blood biomarker HE4 was at a tumor volume of 88 mm^3. (**c**) Distribution of nodule diameters recovered from each mouse at time of positive detection (n = 10 each group). (**d**) Tumor and non-tumor mice were imaged live (top), then sacrificed and the abdominal cavities opened to image tumors without skin attenuation (middle). Visible tumors were resected and mice were imaged again (bottom). (**e**) Luminescence from tumor bearing mice before and after tumor resection was measured, and it was calculated that 17.4% and 17.8% of tumor signal was remaining, respectively. (**f**) Resected tissue is luminescent, suggesting that mostly tumor cells were removed. (**g**) A cell standard OVCAR-8 cells was also imaged, with a limit of detection below 3,000 cells.

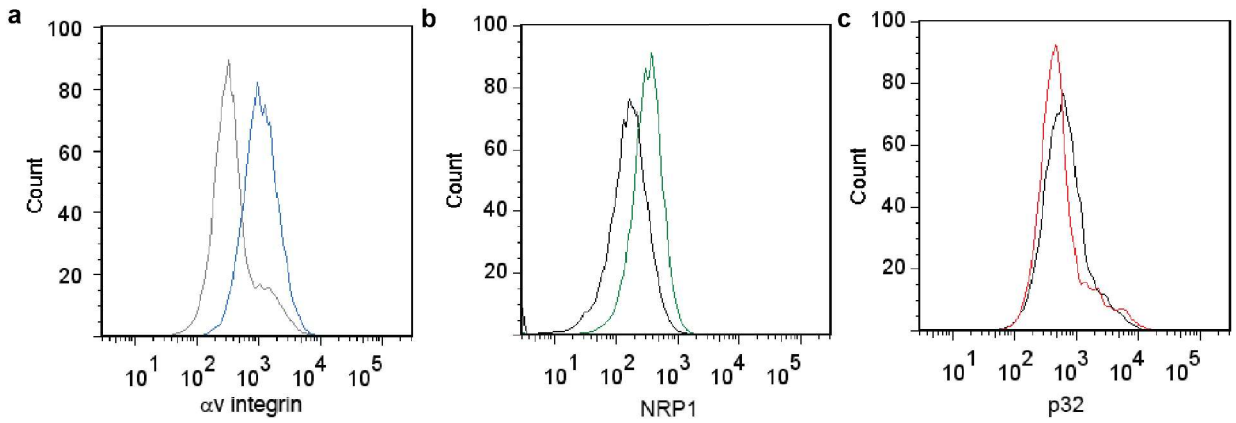

Figure S8. MC26 cell line surface marker analysis by flow cytometry. (**a**) MC26 cells in culture express integrins and (**b**) Neuropilin-1 but not (**c**) p32. Black traces indicate IgG control for each sample.

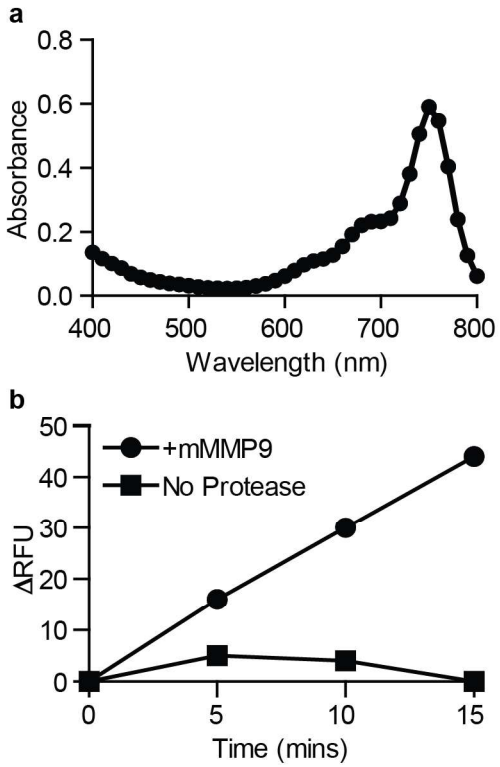

Figure S9. iRGD ABNz characterization. (**a**) Absorbance spectra of iRGD ABNz. Spectra matches LyP-1 ABNz, except iRGD does not have a FAM label. (**b**) Mouse MMP9 is readily able to cleave the selected MMP9 substrate.

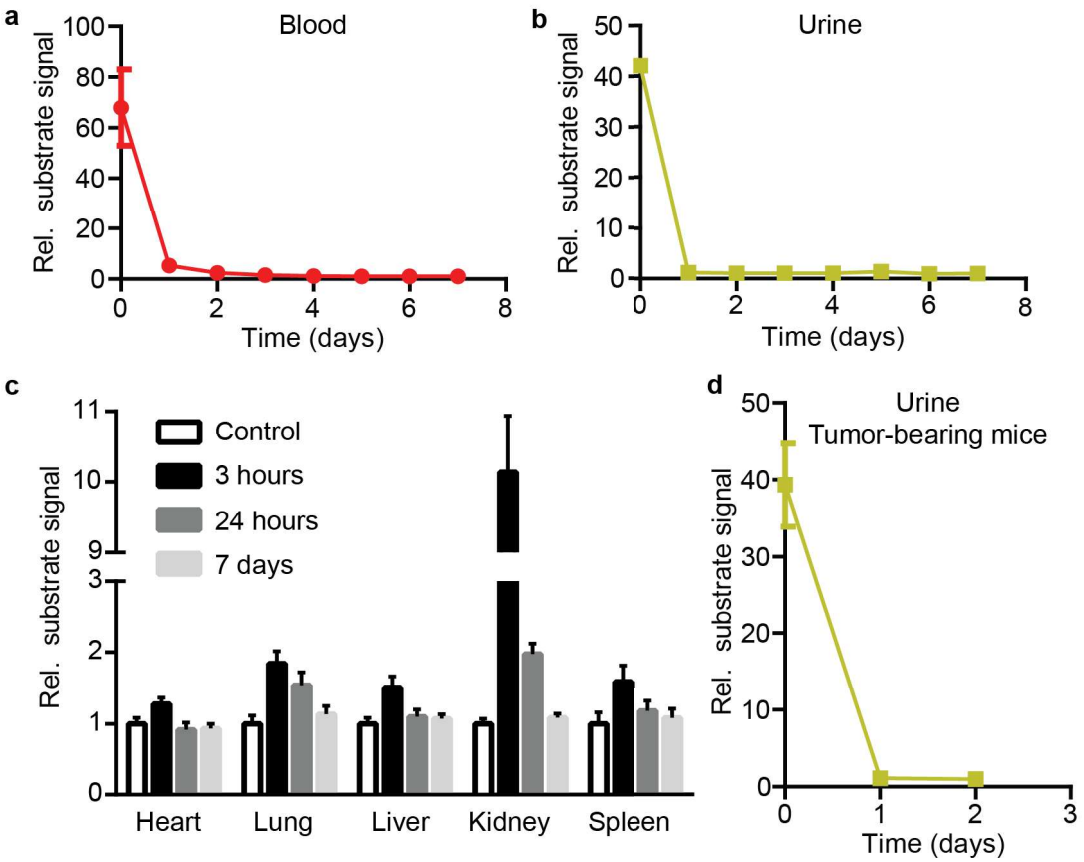

Figure S10. Clearance of ABN in vivo. BALB/c mice were injected with iRGD ABN intravenously and fluorescence was measured in (**a**) blood and (**b**) urine every 24 hours for 7 days. (**c**) Organs were collected 3 hours, 24 hours, and 7 days after ABN administration and fluorescence was measured compared to a PBS injected control. Reporter signal in the blood, urine, and organs was undetectable at 7 days (n = 3, +SEM for all time points). (**d**) Nude mice bearing orthotopic ovarian tumors and injected with ABN have similar urine clearance kinetics with no detectable signal after 1 day (n = 5, ±SEM).

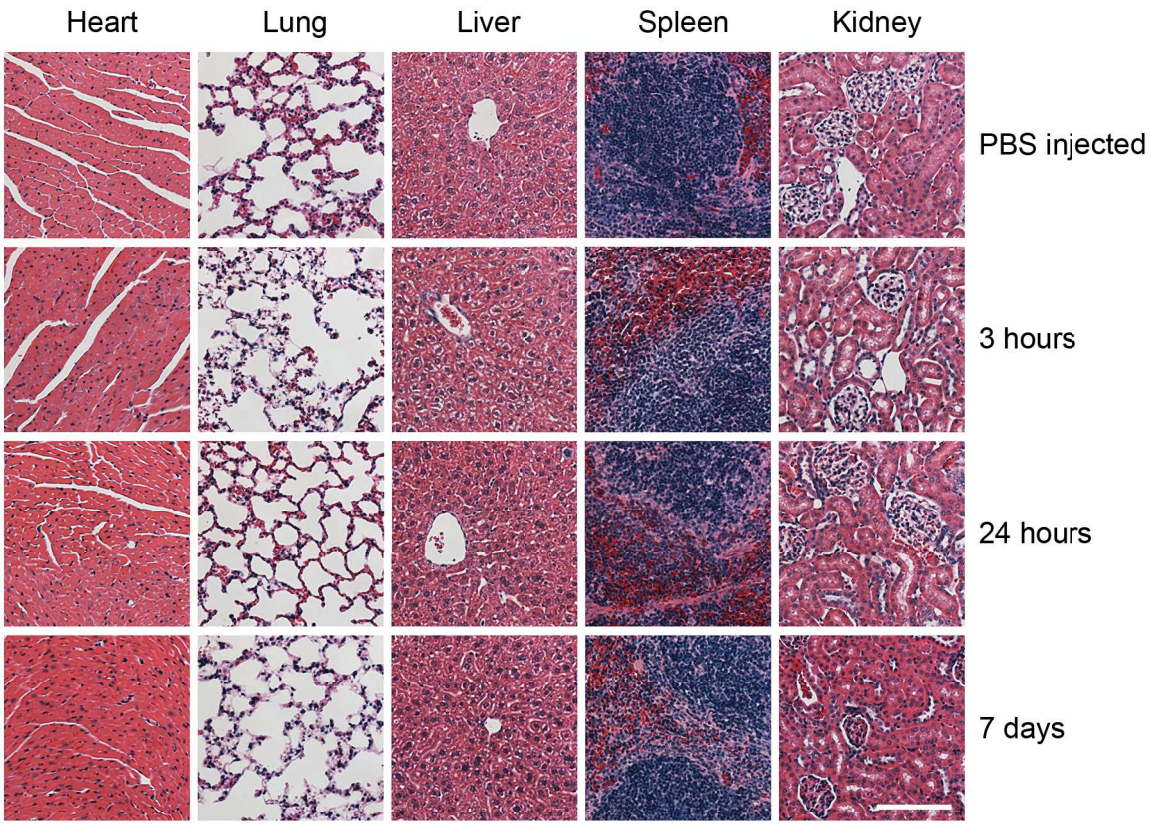

Figure S11. Toxicity of ABN. Immunocompetent BALB/c mice were injected with iRGD ABN, and organs (heart, lung, liver, spleen, and kidney) were collected at 3 hours, 24 hours, and 7 days after administration. Organs were fixed, embedded in paraffin, and stained with hematoxylin & eosin. Analysis by a veterinary pathologist confirmed that tissue from ABN injected animals appeared similar to PBS injected control. Study was done with n = 3 mice and images from a representative animal are shown. Scale bar represents 100 μm.

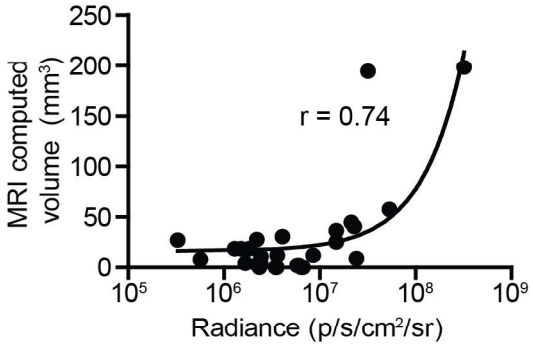

Figure S12. Correlation between MRI computed tumor volume and bioluminescence. MRI and bioluminescence measurements were made by two separate, blinded operators (r: Pearson's correlation).

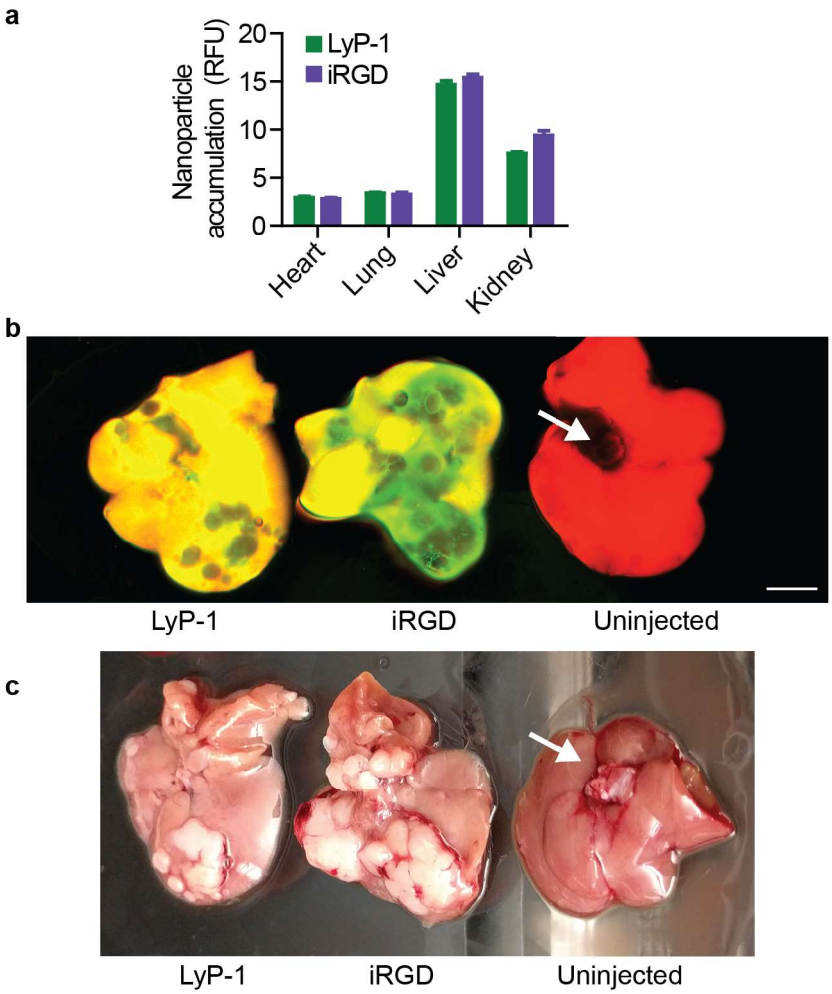

Figure S13. Imaging of nanosensor localization. (**a**) Biodistribution of LyP-1 or iRGD targeted nanoparticles. (**b**) Fluorescent scan of livers with tumor metastases administered iRGD or LyP-1 targeted synthetic biomarkers or uninjected controls. Red = tissue background, green = nanoparticles. Scale bar indicates 2 cm. Uninjected controls show no nanoparticle fluorescence. Tumors are not autofluorescent (white arrow). (**c**) Photograph of excised livers. Tumors are delineated by lack of autofluorescence. iRGD targeted synthetic biomarkers are able to penetrate the tumors more significantly than LyP-1 particles.

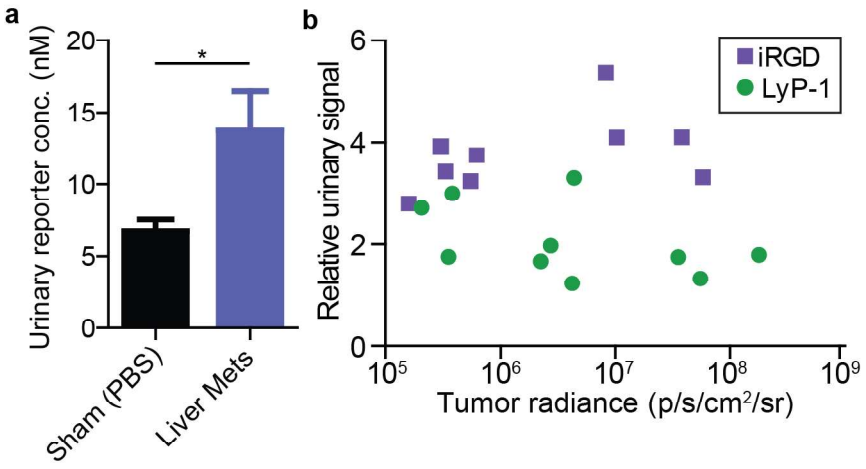

Figure S14. Performance of targeted nanosensors in liver metastasis model. (**a**) iRGD targeted sensors can differentiate liver metastasis bearing mice from age-matched mice that received a sham surgery (n = 5 per condition; ±SEM; Student's *t*-test, two-tailed, **P*<0.05). (**b**) Plot of individual mouse relative urinary signal against tumor luminescence. Tumor luminescence between iRGD and LyP-1 groups were similar.

Supplemental References

1. Kwong, G. A. *et al.* Mathematical framework for activity-based cancer biomarkers. *Proc. Natl. Acad. Sci.* (2015).
2. Hori, S. S. & Gambhir, S. S. Mathematical Model Identifies Blood Biomarker–Based Early Cancer Detection Strategies and Limitations. *Sci. Transl. Med.* **3,** 109ra116–109ra116 (2011).